RSC Advances

PAPER

View Article Online
View Journal | View Issue

Cite this: *RSC Adv.*, 2024, **14**, 3732

Functionalization of *Shorea faguetiana* biochar using Fe_2O_3 nanoparticles and MXene for rapid removal of methyl blue and lead from both single and binary systems†

Aysha Bukhari,[b] Irfan Ijaz,[*b] Ammara Nazir,[b] Sajjad Hussain,[ab] Hina Zain,[c] Ezaz Gilani,[b] Ahmad A. Ifseisi[d] and Hijaz Ahmad[efg]

The synthesis of polymeric magnetic composites is a promising strategy for the rapid and efficient treatment of wastewater. Lead and methyl blue are extremely hazardous to living organisms. The sorption of Pb^{2+} and the dye methyl blue (MB) by biochar is an ecologically sustainable method to remediate this type of water pollution. We functionalized *Shorea faguetiana* biochar with Fe_2O_3 and MXene, resulting in Fe_2O_3/BC/MXene composites with an efficient, rapid, and selective adsorption performance. Based on X-ray photoelectron and Fourier transform infrared spectrometry, we found that the Fe_2O_3/BC/MXene composites had an increased number of surface functional groups (F^-, C=O, CN, NH, and OH^-) compared with the original biochar. The batch sorption findings showed that the maximum sorption capacities for Pb^{2+} and MB at 293 K were 882.76 and 758.03 mg g^{-1}, respectively. The sorption phenomena obeyed a pseudo-second-order ($R^2 = 1$) model and the Langmuir isotherm. There was no competition between MB and Pb^{2+} in binary solutions, indicating that MB and Pb^{2+} did not influence each other as a result of their different adsorption mechanisms (electrostatic interaction for Pb^{2+} and hydrogen bonding for MB). This illustrates monolayer sorption on the Fe_2O_3/BC/MXene composite governed by chemical adsorption. Thermodynamic investigations indicated that the sorption process was spontaneous and exothermic at 293–313 K, suggesting that it is feasible for practical applications. Fe_2O_3/BC/MXene can selectively adsorb Pb^{2+} ions and MB from wastewater containing multiple interfering metal ions. The sorption capacities were still high after five reusability experiments. This work provides a novel Fe_2O_3/BC/MXene composite for the rapid and efficient removal of Pb^{2+} and MB.

Received 24th October 2023
Accepted 25th December 2023

DOI: 10.1039/d3ra07250a

rsc.li/rsc-advances

1. Introduction

Human efforts to fulfill the demands and needs of our growing population—resulting in market growth, technological innovations, capital accumulation, and advancements in living standards—have led to the expansion of many different industries worldwide.[1–5] The heavy metal lead is non-biodegradable in water and accumulates in living organisms, sludges, and sediments, from where it can enter the food chain.[6–8] Human exposure to lead through the consumption of lead-contaminated food and water may affect the nervous system, lungs, and kidneys, and has been linked to hypertension, anemia, peripheral neuropathy, miscarriage, low fertility, cognitive disorders, depressive disorders, and renal damage.[9–14] Organic dyes are used in many different industries, such as the plastics, leather, paper, and textile industries.[15–18] These industries use a lot of water and generate a substantial quantity of colored wastewater. The substance most often used to dye cotton, silk, paper, and leather is methyl blue (MB).[19–21] Positively charged MB can injure human eyes and cause respiratory issues on inhalation; ingesting MB through the mouth can cause vomiting, mental confusion, a burning sensation, profuse sweating, and nausea.[22,23]

Different technologies and approaches are used to remove heavy metals from wastewater, such as ion exchange,

[a]School of Physics, Henan Key Laboratory of Photovoltaic Materials, Henan Normal University, Xinxiang, 453007, China
[b]School of Chemistry, Faculty of Basic Sciences and Mathematics, Minhaj University Lahore, Lahore 54700, Pakistan. E-mail: iffichemixt266@gmail.com
[c]Department of Biological Sciences, Superior University Lahore, Lahore 54700, Pakistan
[d]Department of Chemistry, College of Science, King Saud University, P.O. Box 2455, Riyadh 11451, Saudi Arabia
[e]Center for Applied Mathematics and Bioinformatics, Gulf University for Science and Technology, Kuwait
[f]Department of Computer Science and Mathematics, Lebanese American University, Beirut, Lebanon
[g]Near East University, Operational Research Center in Healthcare, TRNC Mersin 10, Nicosia, 99138, Turkey

† Electronic supplementary information (ESI) available. See DOI: https://doi.org/10.1039/d3ra07250a

evaporation, chemical precipitation, adsorption, reverse osmosis, membrane filtration, flotation, electrochemical deposition, and coagulation–flocculation.[24–33] These approaches have some flaws, such as high operating costs, hazardous byproducts, insufficient removal efficiency, sludge formation, high energy requirements, and difficulties in disposal. Sorption strategies offer advantages over other techniques, such as ease of operation, an outstanding elimination efficiency, affordability, and the ability to regenerate the sorbent.[34] These issues can be resolved by creating an adsorbent with a large surface area, high porosity, greater dispensability, and the correct functional groups.[35–37] The removal of MB from aqueous media before discharge into the environment is important to lessen its influence on living organisms.

A porous, stable, and carbon-rich substance known as biochar (BC) has been prepared and used for various applications, such as soil amelioration, enhancing the biodegradation of organic pollutants or contaminants, and the adsorption of heavy metals.[38–41] For instance, it has been reported that straw or pristine biochar effectively adsorbs Pb^{2+} from water. Biochar synthesized from canola straw was used for the selective elimination of lead from aqueous media; the q_m of lead was 65 mg g^{-1} at a temperature of 500 °C.[42] However, pristine or straw BC shows a lower adsorption of toxic heavy metals, including lead, than modified BC.[43] Consequently, different engineering or modification systems have been used to increase the adsorption capacity of virgin BC.[44] For instance, the binding of BC with nano-materials or metal oxide particles increases the sorption capacity of pristine BC.[45,46] Wang, Yan *et al.* increased the efficiency of BC using an H_2O_2 treatment for lead elimination. The number of functional groups (oxygen) on the BC was enhanced after oxidation by hydrogen peroxide, leading to an increase in the lead sorption capacity (60.87 mg g^{-1}). In other studies, nanoparticles (NPs) or nano-sized materials (*e.g.*, iron, AlOOH, MnO_x, MOS_2, CeO_2, Fe_2O_3, ZrO_2, $La(OH)_3$, and hydroxyapatite) were loaded into BC for use in wastewater remediation.[47–54]

Iron oxide (magnetic) particles or adsorbents are considered to be suitable for solving these issues because they have a high surface area with excellent physiochemical characteristics for metal adsorption and can also be readily isolated using an external magnetic field.[55] However, the direct use of pure or naked magnetic particles or adsorbents may be unsuitable for the removal of metals due to their low surface area, fewer active sites, and low stability without the assistance of covalent linkages. The synergistic coupling of magnetic particles with other adsorbents is considered to be the best way forward for this area of research. A chitosan Schiff base and its magnetic composite have been prepared and applied to the adsorption of pollutants from wastewater.[56,57] Shen, Li, *et al.* reported a highly efficient Fe_2O_3@microalgae composite for the elimination of lead from aqueous media.[58] In another study, a PANI/starch/Fe_2O_3 biocomposite was prepared and used for the adsorption of heavy metals from wastewater.[59]

Since graphene or graphene oxide was prepared from fine graphite powder in 2004,[60,61] 2D materials have attracted attention due to their specific physicochemical and structural features and have been broadly studied in different applications.[62–66] One of the recently developed 2D layered substances is known as MXene, which not has only a large surface area, but also has a more complex chemical composition than graphene[67]. Various researchers have used MXene and its composites for the removal of different environmental contaminants and pollutants.[68] MXene has a rapid and effective adsorption capacity due to the existence of O^-, OH^-, and F^- groups, which provide adsorption sites for positively charged dyes and heavy metals.

An Fe_2O_3/BC/MXene composite has been shown to efficiently, selectively, and rapidly adsorb Pb^{2+} from water, demonstrating that it could be used practically as a new and novel composite to remove ecological contaminants and pollutants. The primary objectives of our research were as follows. First, to functionalize BC using MXene and Fe_2O_3 NPs. MXene provides O, OH, and F cationic groups that enhance the rapid adsorption of anionic lead and MB. The C=O, CN, and OH groups from BC also rapidly absorb Pb^{2+} and MB. Materials belonging to three different categories can therefore be used to design a composite that has a vital role as a novel adsorbent for the rapid, efficient, and selective adsorption of heavy metals, with a >99% removal rate of Pb^{2+} from wastewater. We investigated the influence of the initial MB and lead concentrations, the adsorption time, the initial pH, and the temperature on the adsorption characteristics of the adsorbent. The adsorption was fitted by kinetic, isothermal, and thermodynamic models. The selectivity and reusability of the Fe_2O_3/BC/MXene composite for the adsorption of lead and MB were investigated and the sorption mechanisms were explored.

2. Materials and methods

2.1. Chemicals

The chemicals used are discussed in Text S1 (ESI†).

2.2. Synthesis of Fe_2O_3/BC/MXene

Multi-layered Ti_3C_2 (MXene) materials were prepared by etching the Al from MAX powders using the approach reported by Kong F. *et al.*[69] In a typical synthesis, 4 g of MAX powder were successfully etched using 80 mL of hydrofluoric solution with magnetic stirring at 40 °C for 16 h. The collected suspension was washed with water and subjected to centrifugation at 1500 rpm, producing a dark-colored suspension. Iron oxide NPs were synthesized as reported by Paulson E. *et al.*[70] *Shorea faguetiana* branches were purchased from the native market in Lahore city in Punjab province, Pakistan. The branches of *S. faguetiana* were ground using a grinder, washed with deionized water, and then dried. The biomass was pyrolyzed at 523 K in a muffle furnace for 2 h. The *S. faguetiana* BC was then crushed and passed through a 0.045–0.089 mm sieve and then saved and referred to as virgin BC. The Ti_3C_2 dispersion was sonicated for 1 h. Fe_2O_3 NPs and BC powder were then dropped into the MXene dispersion. To obtain Fe_2O_3/BC/MXene, the resultant product was once more sonicated for 35 min. Fe_2O_3/BC/MXene was isolated by an external magnetic field, rinsed several times

with deionized water to remove impurities, and then dried at 100 °C.

2.3. Characterization

Characterization of the materials is discussed in Text S2 (ESI†).

2.4. Adsorption experiment

The sorption capability and rate of lead and MB removal were determined using eqn (1) and (2) as discussed in Text S3 (ESI†).

$$q_e = \left(\frac{C_o - C_e}{M}\right)V \quad (1)$$

$$R = \left(\frac{C_o - C_e}{C_e}\right) \times 100 \quad (2)$$

2.5. Isothermal study

The Langmuir isotherm equation is expressed as:

$$q_e = \frac{q_{max} K_L C_e}{1 + K_L C_e} \quad (3)$$

The Freundlich isotherm equation is expressed as:

$$q_e = K_F C_e^{\frac{1}{n}} \quad (4)$$

The Dubinin–Radushkevich isotherm model is expressed as:

$$q_e = q_{s\,exp}(-B_\varepsilon^2) \quad (5)$$

The determination and calculation of the Temkin parameters are given as:

$$q_e = \frac{RT}{b}\ln(AC_e) \quad (6)$$

These equations are discussed in Text S4 (ESI†).

2.6. Kinetics analysis

The sorption rate (%) was gauged *via* a pseudo-first-order (PFO) reaction, a pseudo-second-order (PSO) reaction, intra-particle diffusion (IPD), and the Elovich and Bangham diffusion models, as defined in eqn (7), (8), (9), (10), and (11), respectively. The kinetics analysis is discussed in detail in Text S5 (ESI†).

PFO reaction:

$$q_e = (q_e - q_t) = \ln q_e - K_1 t \quad (7)$$

PSO reaction:

$$q_e = \frac{t}{q_e} + \frac{1}{K_2 q_t^2} \quad (8)$$

IPD model:

$$q_e = K_3 t^{0.5} + C \quad (9)$$

Elovich diffusion model:

$$q_t = \frac{1}{\beta}\ln(\alpha\beta) + \frac{1}{\beta}\ln t \quad (10)$$

Bangham diffusion model:

$$\log\log\left(\frac{C_t}{C_t - q_t M}\right) = \log\left(\frac{K_j M}{2.303V}\right) + \alpha \log t \quad (11)$$

2.7. Error functions

To select a suitable kinetic and isothermal model for the Pb^{2+} and MB sorption processes, the sum of the squares of the errors and χ^2 were determined using the following equations:

$$SSE = \sum_{i=1}^{n}\left(f(x_i)_{exp} - f(x_i)_{cal}\right)^2 \quad (12)$$

$$\chi^2 = \sum_{i=1}^{n}\frac{\left(f(x_i)_{exp} - f(x_i)_{cal}\right)^2}{f(x_i)_{cal}} \quad (13)$$

2.8. Thermodynamic study

The thermodynamic parameters were calculated using eqn (14)–(16) and are discussed in detail in the ESI.†

$$K_d = \frac{q_e}{C_e} \quad (14)$$

$$\ln K_d = \frac{\Delta H}{RT} + \frac{\Delta S}{R} \quad (15)$$

$$\Delta G = \Delta H + T\Delta S \quad (16)$$

3. Results and discussion

3.1. Characterization

Fig. 1 shows the FTIR spectra of the Fe_2O_3 NPs, BC, MXene, and the Fe_2O_3/BC/MXene composite. FT-IR was used to explore the essential surface functional groups of the synthesized materials. The Fe–O stretching vibration of the iron oxide NPs is attributed to the peak at 549 cm^{-1}. The OH and C–O–C groups were assigned to bands around 3431 and 1387 cm^{-1}, respectively. The FTIR results for Fe_2O_3 were well matched with a previous study.[71] For BC, there were four bands around 3348, 2930, 1726, 1636, 1557, and 1032 cm^{-1}, which were indexed with the vibration modes of OH, CH, C=O, CN, NH, and CO, respectively. For MXene, there were two typical bands around 675 and 1129 cm^{-1}, indexed to the TiO and F groups. The bands around 3439 and 1641 cm^{-1} were attributed to the hydroxyl and aromatic groups, respectively. Fig. 1 shows the existence of all the major peaks of Fe_2O_3, BC, and MXene in the Fe_2O_3/BC/MXene composite. Fig. 1 also

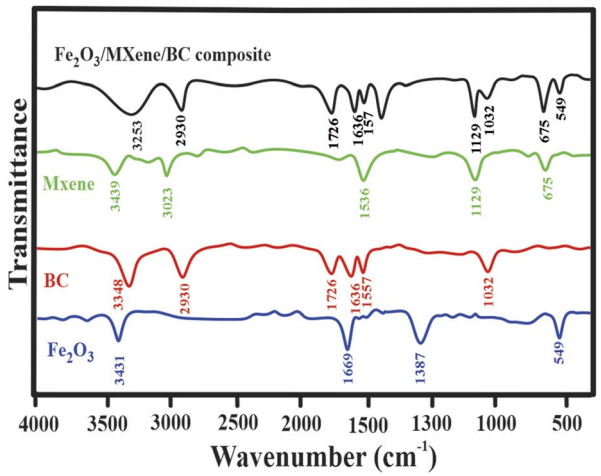

Fig. 1 FTIR spectra of Fe_2O_3 NPs, BC, MXene, and the Fe_2O_3/BC/MXene composite.

shows a broad peak of OH, which may be due to a combination of Fe_2O_3, BC, and MXene.

Fig. 2 shows the XRD patterns of the Fe_2O_3 NPs, BC, MXene, and the Fe_2O_3/BC/MXene composite. For the Fe_2O_3 NPs, the 220, 311, 400, 422, 512, and 440 crystal planes correspond to 2θ values of 30.1, 36.4, 42.90, 53.6, 57.4, and 63.19°, respectively. The XRD pattern indexed well with JCPDS Card #82-1533. Fig. 2 shows that no apparent peak for BC was observed, except for an XRD peak counterpart of an interlayer distance of 0.39 nm at 23°, suggesting that the BC was an amorphous phase. A similar broad peak of BC was also reported by Shan H., *et al.*[72] Specifically, using chemical etching strategies, MXene sheets were obtained *via* the removal of Al layers from the MAX phase with HF. This was confirmed by the substantial shifts found in the XRD peaks. The peak (002) shifted to the left with the disappearance of the characteristic peak of the Ti_3AlC_2 phase at roughly 39° 2θ (Fig. S1†). The typical peaks of MXene at $2\theta = 8.026$, 18.632, 27.458, and 60.821° are attributed to the (002), (006), (008), and (110) crystal planes, respectively.[73] The typical bands of Ti_3C_2 were better in agreement with the result reported by Qi M., *et al.*[74] The composites showed all the characteristic bands of Fe_2O_3 NPs, BC, and MXene (Fig. 2).

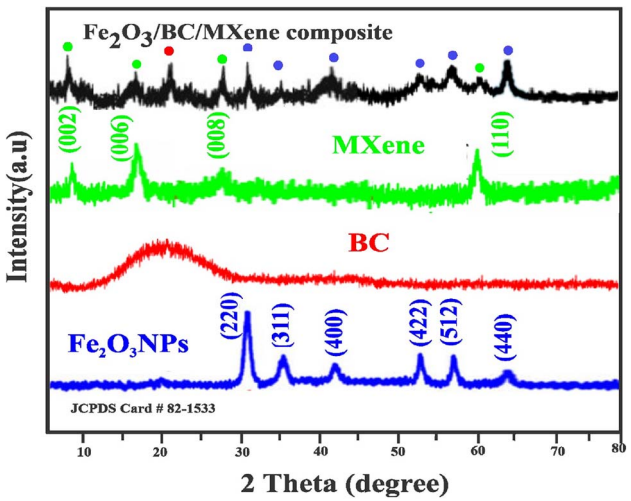

Fig. 2 XRD patterns of BC, MXene, and the Fe_2O_3/BC/MXene composite.

Fig. 3 shows that the saturation magnetization of the composite was 40.24, suggesting paramagnetic behavior. The decrease in the magnetization of the composite could be attributed to the presence of Fe_3O_4 coupled with the non-magnetic features of both MXene and BC. The magnetization features of the composite were sufficient for rapid isolation under an external magnetic field.

Fig. 4(a–i) shows the morphological traits and distribution of elemental species in BC, the Fe_2O_3 NPs, MXene, and the composite determined using SEM, TEM, and EDS. Fig. 4(a) shows the layered structure of MXene. The SEM micrograph in Fig. 4(b) shows the binding of the MXene layers and the Fe_2O_3 NPs with BC. The TEM micrograph in Fig. 4(d) shows iron oxide NPs attached to the surface of the BC. The TEM images in Fig. 4(c) indicate that the MXene layered structure and the Fe_2O_3 NPs bind with BC, in agreement with the SEM results. The EDS patterns in Fig. 4(e–i) show the existence of F, Ti, OH, C, O, and Fe and the homogeneous distribution of elements.

To investigate the sorption process, the binding energies and elemental composition of the Fe_2O_3/BC/MXene composite were determined using the XPS patterns before and after sorption. The Fe_2O_3/BC/MXene composite consists of O, C, H, F, N, Fe, and Ti and confirmed the synthesis of an adsorbent (Fig. 5).

The sorbents exhibited mesoporous characteristics based on the IUPAC classification, as indicated by the type IV isotherms with H_3 hysteresis loops (Fig. S1†). The Fe_2O_3/BC/MXene, BC, MXene, and Fe_3O_4 materials had surface areas of 135.38, 77.091, 51.72, and 49.95 $cm^3\ g^{-1}$, respectively. Fig. S2† indicates that the loading of Fe_3O_4 and MXene increased the surface area of the Fe_2O_3/BC/MXene composite. This increased surface area promoted the diffusion of contaminants during the adsorption process, allowing the more rapid and efficient adsorption of contaminants.[75]

3.2. Adsorption analysis

3.2.1. Influence of pH. The pH of the metal solution is a crucial factor in optimizing adsorption and may influence the speciation of the metal (adsorbate) and the surface charge of the adsorbent. The protonation–deprotonation process of reactive substances at the surface of the adsorbent may cause an attraction–repulsion effect. To explore the influence of pH on the adsorption of Pb^{2+} and MB on the composite, the elimination (%) of Pb^{2+} and MB was investigated by batch experiments at pH 1–11 (Fig. 6(a and b)). The removal (%) of lead increased rapidly as the pH increased from 2 to 3.7, slowly increased from pH 3.7 to 4.6, and then remained nearly constant until pH 6. A similar pattern has been reported previously.[76] Above pH 6, the removal (%) of lead gradually decreased until pH 10. An increase in elimination with an increase in the pH caused by the deprotonation of active groups provides sites for the sorption of lead. The linear plot for pH 4.6–6 describes the saturation of the surface with lead. Depending on the pH, lead ions in aqueous solution can form various hydroxides.[77]

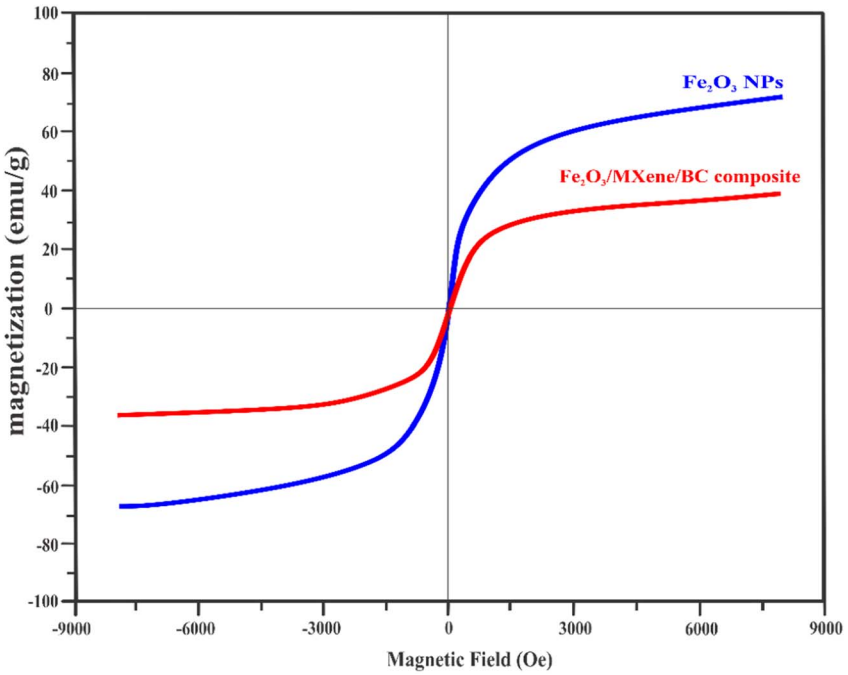

Fig. 3 Magnetization curves of Fe_2O_3NPs and Fe_2O_3/BC/MXene.

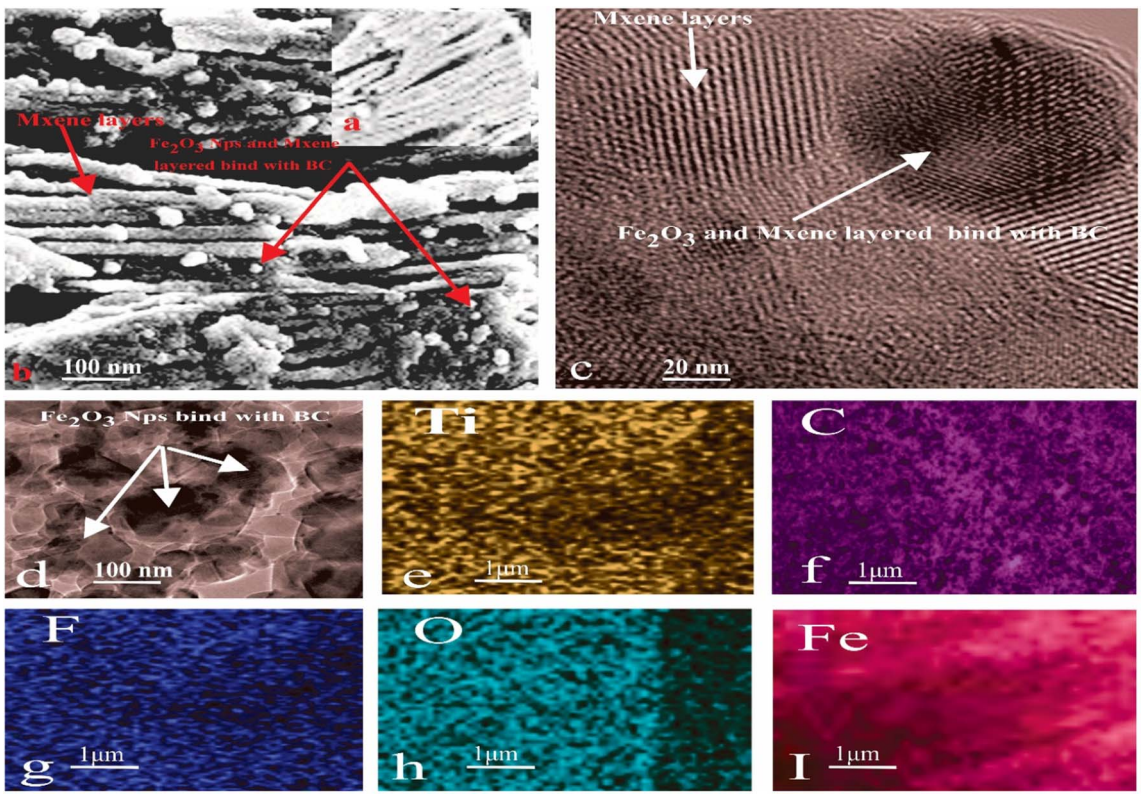

Fig. 4 (a, b) SEM and (c, d) TEM images of the composites and (e–i) EDS spectra of Fe_2O_3/BC/MXene.

$$Pb^{2+} \leftrightarrow Pb(OH)^{+} \leftrightarrow Pb(OH) \leftrightarrow Pb(OH)_3^{-} \leftrightarrow Pb(OH)_4^{2-} \quad (17)$$
$$\rightarrow \rightarrow$$

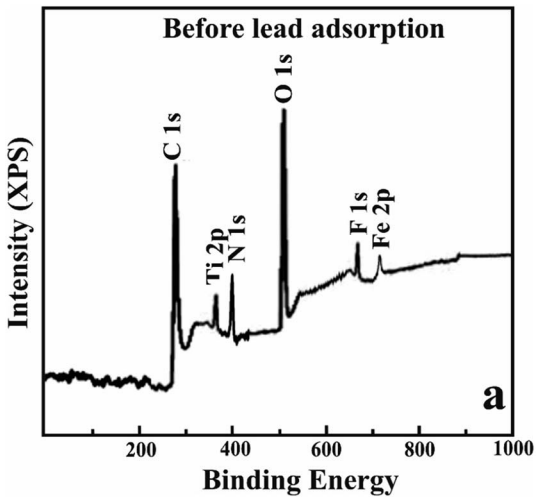

Fig. 5 XPS survey of the Fe_2O_3/BC/MXene composite.

Precipitates were formed in an aqueous solution of lead above pH 6, suggesting that elimination above pH 6 was due to both the precipitation of lead as $Pb(OH)_2$ and adsorption as Pb^{2+} and $Pb(OH)^+$ ions. The decrease in the elimination of lead above pH 10 was caused by an increase in the concentration of $Pb(OH)_4^{2-}$ and $Pb(OH)_3^-$ due to repulsion between the anionic composite and $Pb(OH)_3^-$ and $Pb(OH)_4^-$ at high pH values. The pH-based zeta potential of the composite is shown in Fig. 6(b). The Fe_2O_3/BC/MXene composite had a positive charge at pH values <2.2 and the surface charge changed to negative. As a result, a change in pH from 2.2 to 9 caused an increase in the removal rate of MB.

The zeta potential is zero at the iso-electronic point. Fig. 6(c) shows that the pH_{zpc} of the composite was 2.2, suggesting that the Fe_2O_3/BC/MXene composite had no surface charge at pH 2.2. The surface of the composite was positively charged below pH 2.2, but changed to a negative charge at pH values above 2.2.

3.2.2 Effect of sorption time and kinetic analysis. An essential characteristic of a prepared sorbent is the adsorption time. We explored the kinetics by examining the adsorption equilibrium time at three different temperatures (293, 303, and 313 K). The kinetics for the adsorption of MB and Pb^{2+} by Fe_2O_3/BC/MXene were explored at different adsorption times. Fig. 7(a) shows that the adsorption capacity of the composite for MB and lead ions increased rapidly within 16 min due to the presence of sufficient adsorbent on the Fe_2O_3/BC/MXene composite. The adsorption capability of the adsorbent increased gradually for the first 21 min, indicating that the movement of Pb^{2+} ions and MB attained equilibrium after the major sorption sites had been filled.

The kinetic sorption of MB and Pb^{2+} by the Fe_2O_3/BC/MXene composite could be fitted by the PFO, PSO, and IPD kinetics models (Fig. 7(b–d)) using eqn (7), (8), and (9). Table S1† shows

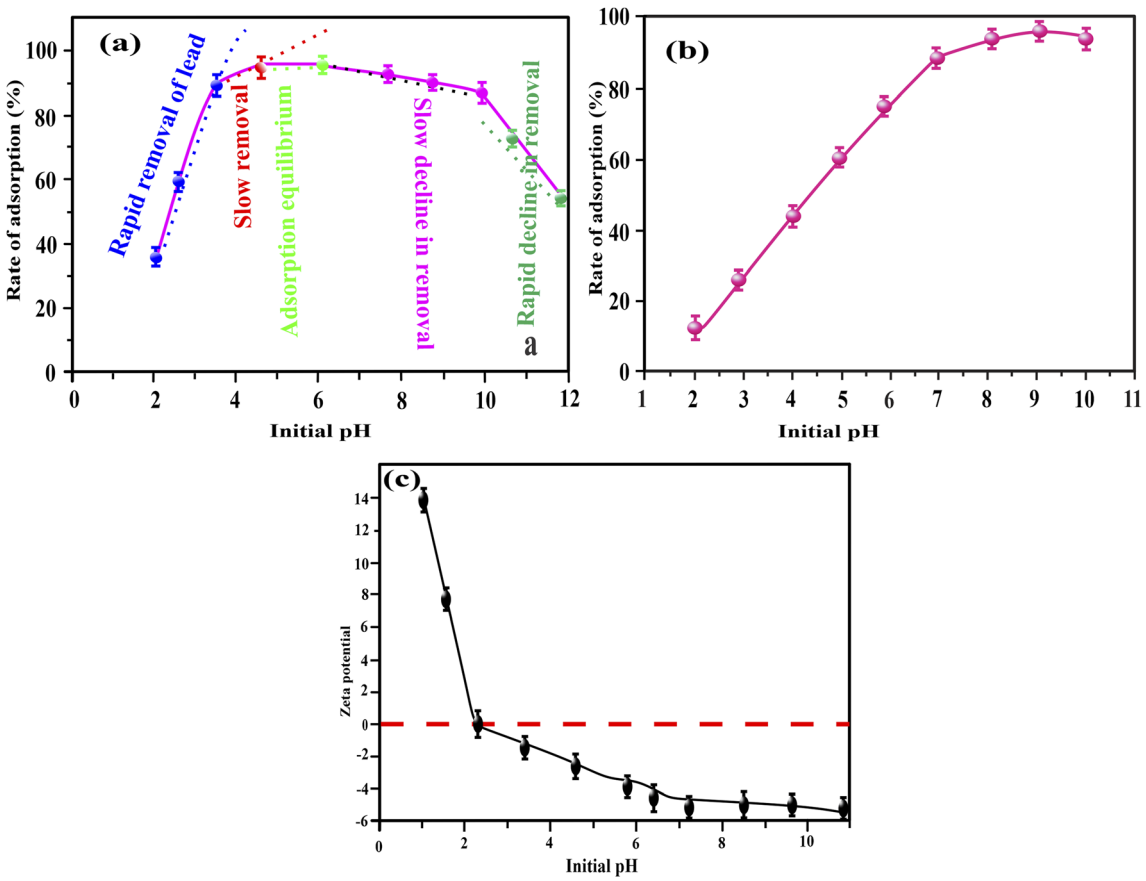

Fig. 6 Influence of the initial pH on the adsorption of (a) Pb^{2+}, (b) MB, and (c) the zeta potential of Fe_2O_3/BC/MXene.

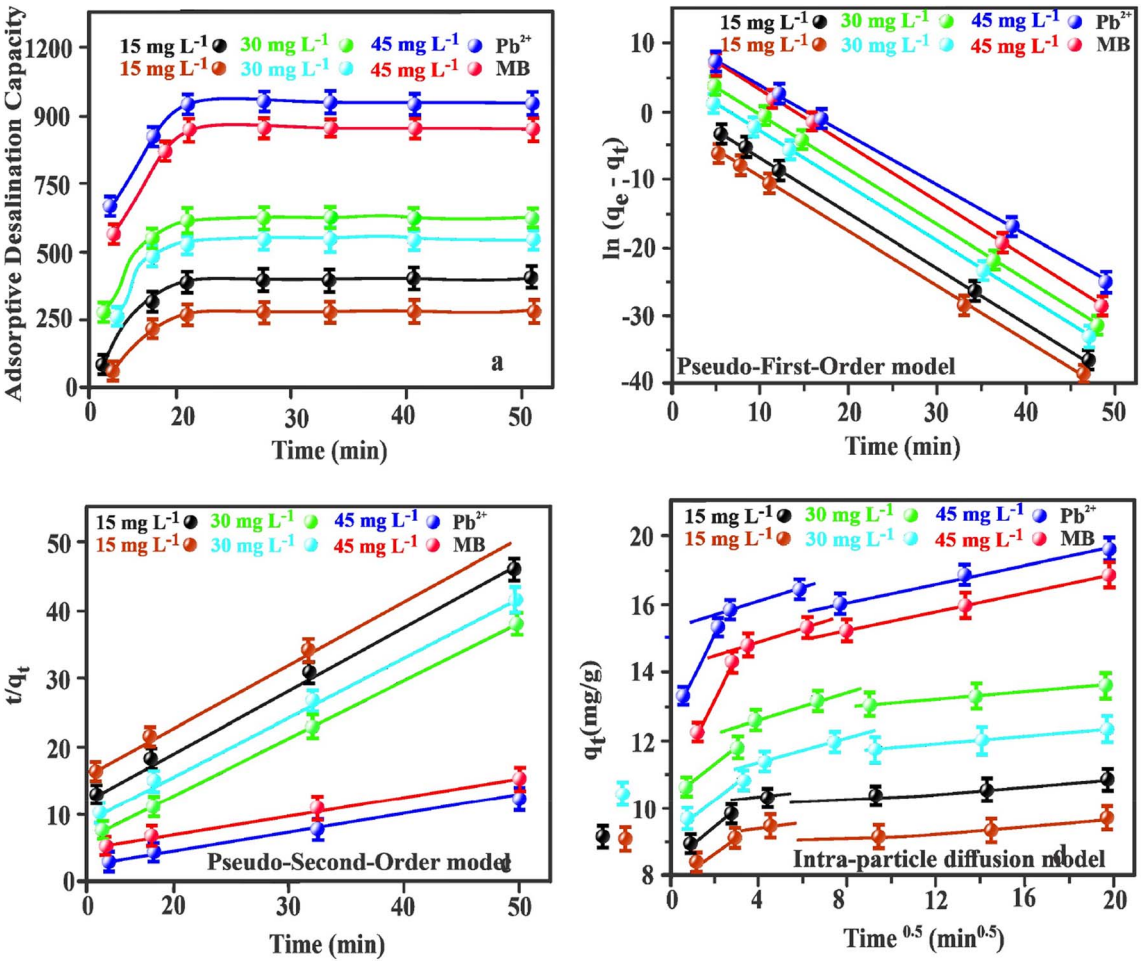

Fig. 7 Influence of (a) adsorption time for the (b) PFO, (c) PSO, and (d) IPD models.

that the correlation coefficients (Pb^{2+}: $R^2 = 1$; MB: $R^2 = 0.997$) of the PSO model for the composite were greater than those of the PFO model (Pb^{2+}: $R^2 = 0.9326$; MB: $R^2 = 0.9183$). Higher values of the correlation coefficients and lower values for χ^2 and the SSEs showed the better suitability of the PSO model. The q_e values of the composite derived from the PSO kinetic model were comparable with the experimental values. Hence the sorption process of the composite for Pb^{2+} and MB could be explained by the PSO kinetic model, suggesting that chemical adsorption occurred between the prepared Fe_2O_3/BC/MXene composite and the Pb^{2+} ions and MB.[78]

The Elovich kinetic model is an efficient strategy for elucidating the mechanism of sorption of gases onto the surface of solids. It is widely used in a number of different applications, especially the adsorption of pollutants from aqueous solutions.[79] The Elovich model exhibited practical suitability in fitting the kinetic experimental data for Pb^{2+} and MB ($R^2 = 0.996$ and 0.991, respectively) (Fig. S3(a)†). The greater α_{El} values acquired for the Fe_2O_3/BC/MXene composite demonstrate rapid chemisorption due to the porous nature of the synthesized composite.

The Bangham kinetic model was formulated under the hypothesis that the rate-limiting step in the sorption phenomenon is due to pore diffusion. Using eqn (11), the double logarithmic plot (Fig. S3(b)†) produced linear curves showing significant correlation coefficients (R^2) of 0.981 and 0.969 for Pb^{2+} and MB, respectively. This shows that pore diffusion greatly affects the rate-controlling step.

The IPD model was also used to investigate intra-particle diffusion between Pb^{2+} and MB and Fe_2O_3/BC/MXene composite. Fig. 7(d) shows the association between q_t and $t^{1/2}$ of the Pb^{2+} and MB dose by the Fe_2O_3/BC/MXene composite, which was non-linear throughout the time range. The outcome obtained suggests that the adsorption mechanism is not impacted *via* monolayered diffusion parameters.[80] The entire diffusion process is divided into three linear areas that demonstrate surface sorption, membrane diffusion, and IPD. By observing the fundamental parameters of IPD at different concentrations (Table S2†), we found that KI and CI were larger than KII and KIII and CII and CIII, respectively. After three sorption stages, the sorption sites on the adsorbent gradually decrease and the sorption rate (%) also gradually decreases. KI for both pollutants was greater than KII and KIII due to the reduced number of active sites on the Fe_2O_3/BC/MXene with increasing time. The steadily decreasing K readings showed that the diffusion rate had slowed and that chemisorption was becoming balanced. The effect of the boundary layer increased with increasing *c* values.

3.2.3. Influence of initial concentration of lead and isothermal analysis. The influence of the initial dose of both pollutants was examined to study the q_m of the Fe_2O_3/BC/MXene composite for MB and Pb^{2+}. Fig. 8(a) represents the q_m values of Fe_2O_3/BC/MXene for Pb^{2+} ions and MB at 293, 303, and 313 K. The maximum adsorption capacity of the Fe_2O_3/BC/MXene composites was at 293 K. With an increase in the dose of pollutants, the sorption capability slowly increased and eventually reached an equilibrium. The increased concentrations of Pb^{2+} and MB enhanced the possibility of contact between Pb^{2+} and MB with the surface-active groups of the Fe_2O_3/BC/MXene composite, further enhancing the adsorption process. The number of active sites or contact points on the Fe_2O_3/BC/MXene composite was limited. All the contact points or active sites of the sorbent had been used when the Pb^{2+} and MB concentrations accumulated to a specific degree and the prepared sorbent attained a saturation state, above which the removal capacity no longer increased. Fig. 8 shows that the sorption capability of Fe_2O_3/BC/MXene for Pb^{2+} and MB decreased as the temperature increased, demonstrating that the sorption phenomena is exothermic.

The adsorption isotherms of MB and Pb^{2+} by Fe_2O_3/BC/MXene using non-linear fitting are shown in Fig. 8(a and b) and the associated parameters are listed in Table S3.† These findings show that the Langmuir model gave a better fit than the Freundlich and Temkin isothermal models, with higher R^2 values for both Pb^{2+} and MB. The fitting of the Langmuir model defines the single-layer, homogeneous adsorption of Pb^{2+} ions and MB onto Fe_2O_3/BC/MXene composite.[81] The maximum sorption capacities of the Fe_2O_3/BC/MXene composite toward Pb^{2+} and MB were 882.76 and 758.03 mg g^{-1}, respectively, which are higher than those for previously reported adsorbents. Furthermore, the calculated sorption capacity at 293, 303, and 313 K (882.76, 613.37, and 305.06 mg g^{-1}, respectively) for Pb^{2+} from the Langmuir model was close to the experimental adsorption capacity (885, 620, and 310 mg g^{-1}). The calculated sorption capacities for MB (758.03, 562.91, and 296.88 mg g^{-1}, respectively) obtained from the Langmuir isotherm model were also close to the experimental adsorption capacities (760, 570, and 300 mg g^{-1}) at 293, 303, and 313 K, respectively.

3.2.4. Simultaneous removal of Pb^{2+} ions and MB. Pb^{2+} and MB were adsorbed simultaneously at environmentally relevant amounts. By calculating the maximum adsorption capacities ratio (R_q), we investigated the impact of both Pb^{2+} and MB in single and binary processes to better understand their synchronous adsorption:

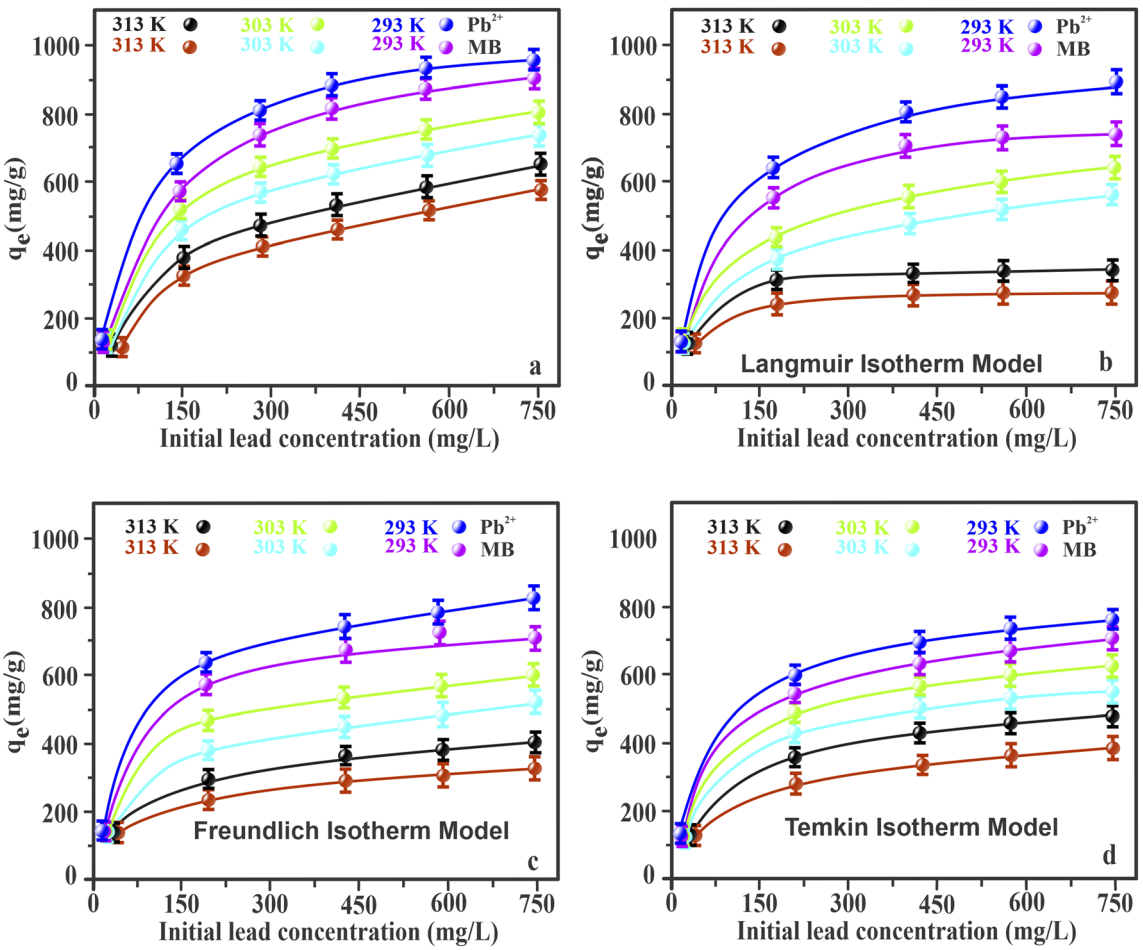

Fig. 8 Influence of Pb^{2+} dosages on the adsorption capability of Fe_2O_3/BC/MXene (a) using Langmuir (b), Freundlich (c), and Temkin (d) models.

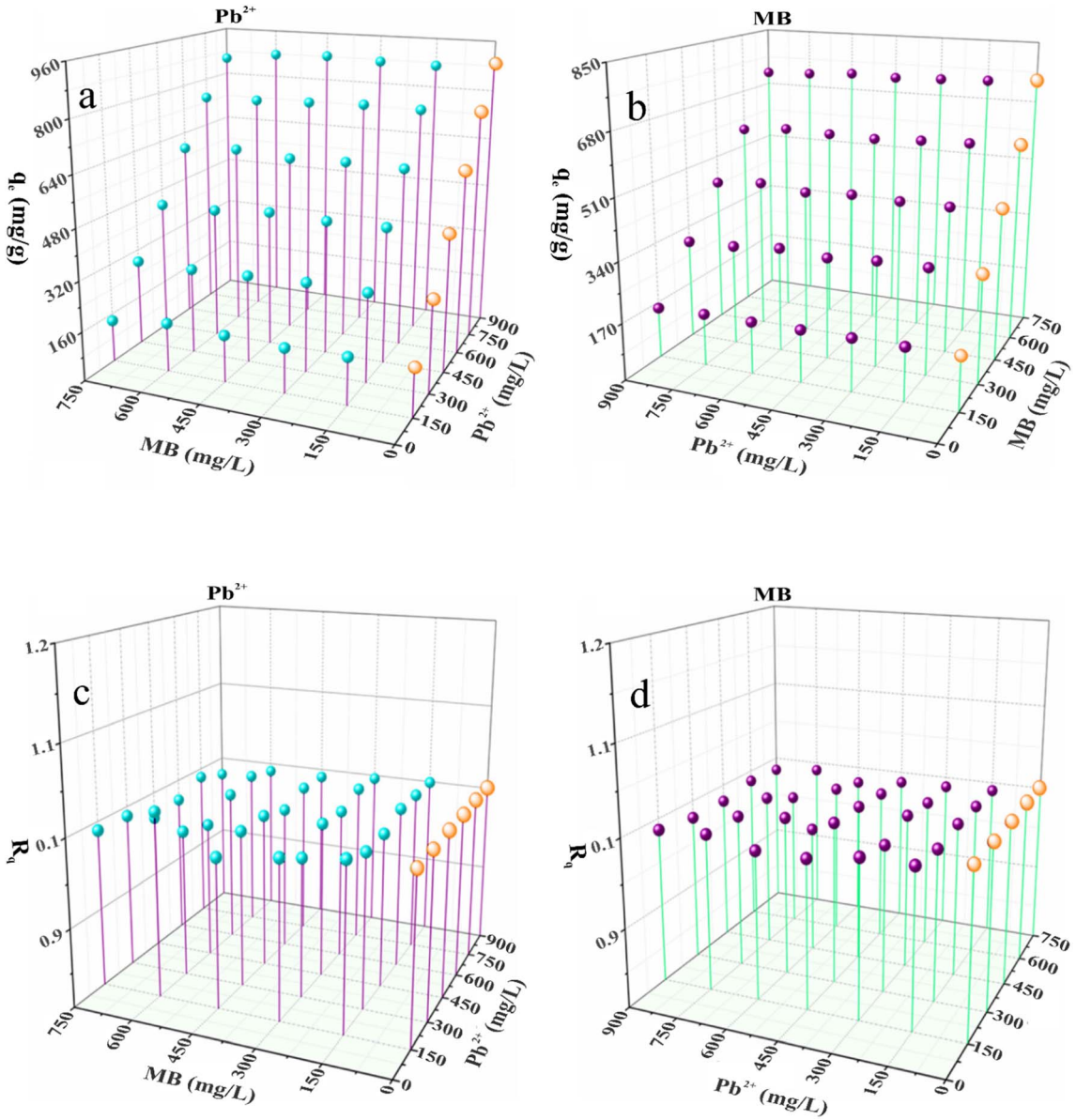

Fig. 9 (a, b) Simultaneous adsorption of Pb(II)–MB by the Fe_2O_3/BC/MXene composites using the binary system (Pb(II) + MB) and (c, d) their R_q values. The single-pollutant system (orange spheres) was used as a reference.

$$R_q = \frac{q_{b,i}}{q_{m,i}} \quad (18)$$

where $q_{m,i}$ and $q_{b,i}$ denote the adsorption capacity (mg g^{-1}) in single and binary solutions at the same initial dose. If $R_q < 1$, then adsorption is suppressed due to the presence of coexisting contaminants (antagonism). If $R_q > 1$, then contaminant adsorption is enhanced due to the presence of co-contaminants. If $R_q = 1$, then the co-contaminants did not influence the adsorption of the contaminant.

Fig. 9(a–d) shows the results of the simultaneous examination of Pb–MB adsorption on the Fe_2O_3/BC/MXene composite. The contaminant adsorption curves in the single-pollutant system are also shown as a reference (orange spheres). These outcomes indicate that the elimination of MB and Pb from the binary solution was analogous to that from the single-pollutant systems (MB and Pb^{2+}) with R_q values close to 1 (Fig. 9(c and d)). The synergistic interaction is probably explained as follows. According to the adsorption results in the single-pollutant system, the MB and Pb^{2+} absorption modes were different (electrostatic interaction for Pb^{2+} and hydrogen bonding for MB). Consequently, there is no competition between MB and Pb^{2+} in the binary solution. These outcomes indicate that MB and Pb^{2+} did not influence each other as a result of their different adsorption mechanisms (Fig. 10(a and b)).

3.2.5. Influence of temperature and thermodynamics. Temperature is a primary variable in the remediation capacity of the adsorption process. The influence of the temperature on the adsorption of Pb^{2+} and MB by the Fe_2O_3/BC/MXene composite was therefore investigated (Fig. 10(a and b) and

Table S4†). To evaluate whether the adsorption of the Pb^{2+} ions and MB by the composite was exothermic or endothermic, the thermodynamic characteristics of the reaction were examined in the temperature range 293–313 K. An increase in the temperature adversely influenced the percentage removal of the sorption phenomena, demonstrating the exothermic nature of the procedure. The decrease in the sorption capacity may be connected to the modification (denaturing) of the sorbent at high temperatures, which causes a reduction in the number of sites. The adsorbed Pb^{2+} ions and MB on the surface of Fe_2O_3/BC/MXene could escape with increasing temperature.[82] $\Delta H <$ 0 shows that the adsorption of metal ions and dye on the Fe_2O_3/BC/MXene composite was exothermic. The negative ΔG at various temperatures and $-\Delta G$ increase with increasing temperatures indicate the sorption of Pb^{2+} ions and MB was both feasible and spontaneous. The negative value of entropy indicates that the solid–liquid interface was less random and irregular and that the adsorption process took place under unfavorable environmental conditions.

3.2.6. Adsorption selectivity. The selective sorption of Pb^{2+} ions using the Fe_2O_3/BC/MXene composite was explored and comparative experiments were performed to determine the selectivity of BC/MXene and BC/Fe_2O_3. Wastewater containing Cu^{2+}, Pb^{2+}, Li^{1+}, Zn^{2+}, Mg^{2+}, and Cd^{2+} was adjusted to a pH of 4.5 and 20 mg of the composite and 20 mg of aqueous media were mixed in a centrifuge tube and left to react for 12 h before isolating the solid from solvent. ICP-AES was used to determine the concentration of Pb^{2+} before and after sorption. Table S5 and Fig. S4† show the adsorption results for BC/MXene, BC/Fe_2O_3, and Fe_2O_3/BC/MXene. BC/MXene and BC/Fe_2O_3 had a lower selectivity and lower adsorption for Pb^{2+} ions in wastewater. Fe_2O_3/BC/MXene was more selective and the sorption process was more promising than that for BC/MXene and BC/Fe_2O_3. The distribution (K_d) and selectivity (K) coefficients were used to understand the selective adsorption of Pb^{2+} in solution using adsorbents. K_d and K can be described by eqn (14) and (15).

$$K_d = \frac{q}{c_e} = \frac{C_o - C_e}{C_e}\frac{V}{M} \quad (19)$$

$$K = \frac{K_{d(Pb^{2+})}}{K_{d(coeixtingions)}} \quad (20)$$

The results are displayed in Table S5 and Fig. S4.† For the BC/MXene, BC/Fe_2O_3, and Fe_2O_3/BC/MXene adsorbents, the K_d values of Pb^{2+} were higher than for other heavy metal ions in simulated wastewater and showed the strongest interaction between Pb^{2+} ions and the adsorbent. The percentage removal rate was higher than for other metal ions. The tables also suggest that BC/MXene and BC/Fe_2O_3 showed a higher value of K than Fe_2O_3/BC/MXene for interfering ions, suggesting that the functional groups have less affinity for mixed ions. We conclude that Pb^{2+} ions can be selectively and efficiently eliminated from wastewater using the Fe_2O_3/BC/MXene composite.

3.2.7. Reusability of the Fe_2O_3/BC/MXene composite. It is crucial to determine the reusability of the prepared adsorbent because, in real-world situations, the cost of consumption should be considered. The findings at pH 4.5 for Pb^{2+} and pH 9 for MB (at 298 K) are shown in Fig. S2.† The sorption capacity of the first replicated trial for Pb^{2+} was 99.91% and remained at 90.99% after five successive cycles. By contrast, the sorption capacity of the first replicated trial for MB was 98.63% and remained at 89.47% after five successive cycles. The desorption trials also suggest that the composite is an excellent adsorbent for Pb^{2+} ions and the desorption efficiency only decreased from 96.8 to 78.32% after five trials (Fig. S5(a)†). The desorption trials suggested that the composite had excellent adsorption for MB and the desorption efficiency only decreased from 95.08 to 77.40% after five trials (Fig. S5(b)†).

3.2.8. Adsorption mechanism. Fig. 11 shows the FTIR spectra of the Fe_2O_3/BC/MXene composite, Fe_2O_3/BC/MXene–Pb, and Fe_2O_3/BC/MXene–MB. Three areas show clear changes in the FTIR pattern of Fe_2O_3/BC/MXene–Pb, and Fe_2O_3/BC/MXene–MB. The first area is at about 3300–3200 cm^{-1}, attributed to OH and NH stretching in the composite moving to lower wavenumbers. This suggests an increase in bond length due to the variation in the electronegativity of the neighboring atoms—for instance, hydrogen bonding, which can also be observed in Fig. 11. In the second area (1050–1750 cm^{-1}), the bands around 1726, 1636, and 1129 cm^{-1} move to lower wavenumbers for Pb^{2+} (1709, 1618, and 1098 cm^{-1}, respectively), MB^{+} (1715, 1627, and 1109 cm^{-1}, respectively), and Pb^{2+}–MB (1703, 1622, and 1121 cm^{-1}, respectively), indicating that C=O, CN, and F interact (electrostatic interactions) with Pb^{2+}, MB, and Pb^{2+}–MB^{+} due to differences in polarity (Fig. 12). In the third area (500–900 cm^{-1}), the band at

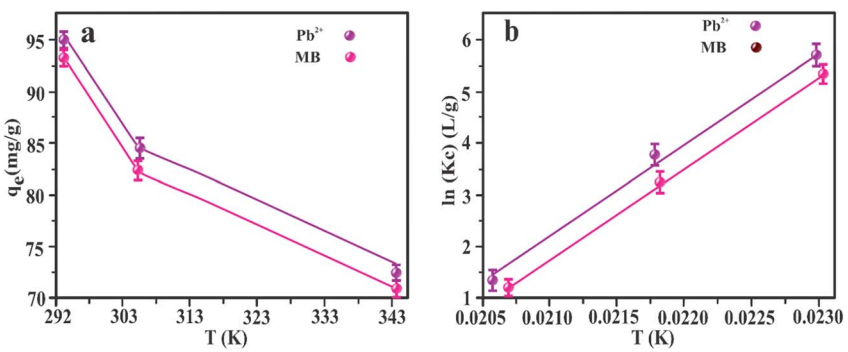

Fig. 10 (a) Influence of temperature on adsorption and (b) plot of ln K_c *vs.* 1/T.

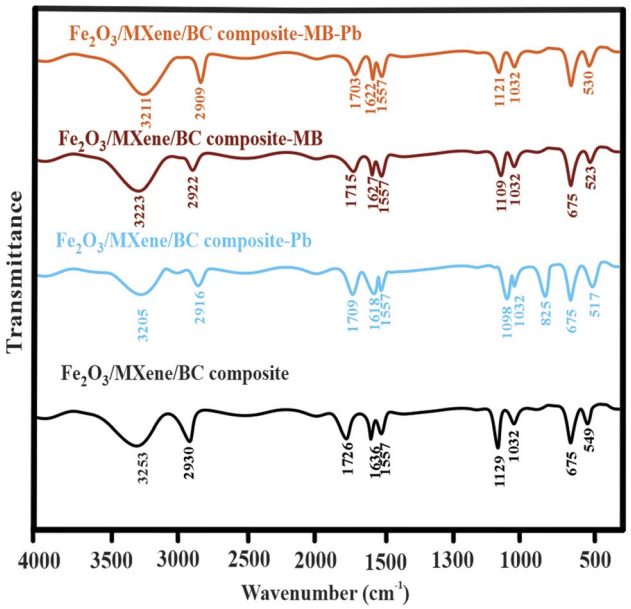

Fig. 11 FTIR patterns of the Fe_2O_3/BC/MXene–Pb and Fe_2O_3/BC/MXene–MB composites before and after the adsorption of Pb^{2+}, MB, and Pb^{2+}–MB.

549 cm^{-1} corresponding to the FeO stretching vibration of iron oxide NPs moved to a lower wavenumber for Pb^{2+} (517 cm^{-1}), MB (523 cm^{-1}), and Pb^{2+}–MB^{+} (530 cm^{-1}) and became weaker, which indicates the interaction (oxido-reduction) of FeO with Pb^{2+}, MB, and Pb^{2+}–MB. A further band appeared at 825 cm^{-1} corresponding to PbO, similar to the band also reported previously.[83]

The presence of Pb^{2+} in the XPS pattern of Fe_2O_3/BC/MXene–Pb verified the successful adsorption of Pb^{2+} (Fig. S6(a)†). The existence of Pb^{2+} in the XPS pattern was confirmed at a binding energy of about 143.17 (Pb4f 5/2) and 139.23 eV (Pb4F 7/2) (Fig. S6(b)†). Similarly, the presence of S in the XPS pattern of Fe_2O_3/BC/MXene–MB showed the successful adsorption of MB (Fig. S6(c)†). The O 1s XPS bands at 532.3 and 533.5 eV correspond to C–OH and C=O, respectively, before adsorption (Fig. S7(a)†). After the adsorption of Pb^{2+}, MB, and Pb^{2+}–MB (simultaneous removal), there was a slight movement of the bands at 532.3 eV (C–OH) to 532.5 eV (Pb^{2+}), 533.8 eV (MB), and 533.0 eV (Pb^{2+}–MB), which indicated the interaction of the hydroxyl group with Pb^{2+} and MB. After the adsorption of Pb^{2+}, MB, and Pb^{2+}–MB (simultaneous removal), there was a slight movement of the bands at 533.5 eV (carbonyl oxygen) to 533.7 eV (Pb^{2+}), 533.9 eV (MB), and 533.6 eV (Pb^{2+}–MB), respectively, which indicated the interaction of the carbonyl oxygen with Pb^{2+} and MB and the simultaneous removal of lead and MB (Fig. S7(a)†).

Three peaks appeared at 284.3, 285.3, 287.5, and 288.6 eV, correlating to the C–C, C=C, C–O, and C–F groups of the composite, respectively (Fig. S7(b)†). The peaks at 284.3, 285.3, 287.5, and 288.6 eV correspond to C–C, C=C, C–O, and C–F shifting to the binding energies for Pb^{2+} (284.5, 285.6, 287.7, and 288.8 eV), MB (284.9, 285.5, 287.9, and 288.9 eV), and Pb^{2+}–MB (284.7, 285.8, 287.8, and 289.0 eV), suggesting that the C–C, C=C, C–O, and C–F of the composites provided a binding site for Pb^{2+} and MB adsorption as well as the simultaneous removal of lead and MB (Fig. S7(b)†).

The N 1s XPS bands at 398.0, 398.7, and 399.6 eV correspond to the C=N, C–N, and NH groups before adsorption (Fig. S7(i)†). After the adsorption of Pb^{2+}, MB, and Pb^{2+}–MB (simultaneous removal), there was a slight shift from 398.0 eV (C=N) to 398.4 eV (Pb^{2+}), 398.2 eV (MB), and 398.5 eV (Pb^{2+}–MB), indicating the interaction of the C=N group of Fe_2O_3/BC/MXene with both pollutants. After the adsorption of Pb^{2+}, MB, and Pb^{2+}–MB (simultaneous removal), there was a slight shift from 398.7 eV (C=N) to 398.9 eV (Pb^{2+}), 399.1 eV (MB), and 399.3 eV (Pb^{2+}–MB), which indicates the interaction of the C–N group of Fe_2O_3/BC/MXene with both pollutants. Similarly, after the adsorption of

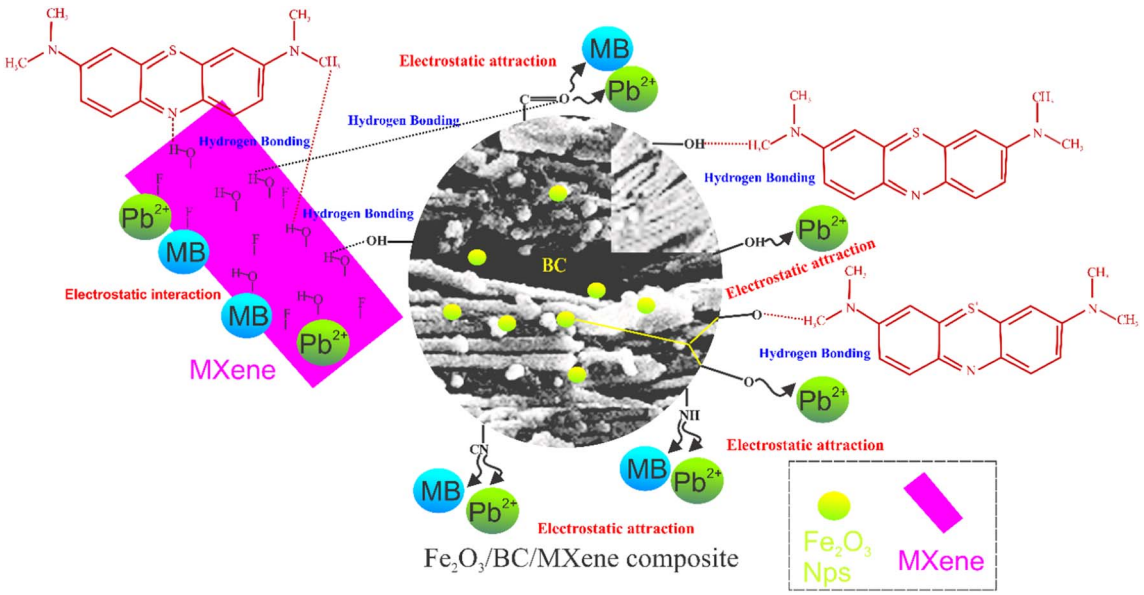

Fig. 12 Possible mechanism of adsorption of Pb^{2+} onto the Fe_2O_3/BC/MXene composite.

Table 1 Comparative analysis of the removal of Pb^{2+} by Fe_2O_3/BC/MXene and previously reported adsorbents

Adsorbent	Adsorption capacity (mg g^{-1})	Temperature	pH	Reference
Pb^{2+}				
$KMnO_4$-modified BC	37.51	22 °C	5	84
MoO_3–BC	229.87	315 K	4.0	85
$MnSO_4 \cdot 4H_2O$ peanut shell BC	68	45 °C	5.0	.[86]
Magnetic oak bark BC	30	25 °C	7.7	87
CeO_2–MoS_2 hybrid wood BC (600 °C)	263.6	—	4.0–4.2	48
Fe_2O_3/BC/MXene	992	293 K	4.5	This work
MB				
Olive pomace boiler ash	149.11	30 °C	3–7	88
Ultrasonic acid modification of raw olive pomace	25.64	303 K	3–12	89
Manganese-modified lignin BC	248.96	—	3–11	90
Magnetic BC synthesized with waterwork sludge and sewage sludge	186.003	—	—	91
Fe_2O_3/BC/MXene	899.03	293 K	3–9	This work

Pb^{2+}, MB, and Pb^{2+}–MB (simultaneous removal), there was a slight shift from 399.6 eV (NH) to 399.8 eV (Pb^{2+}), 400.0 eV (MB), and 400.2 eV (Pb^{2+}–MB), which indicates the interaction of the NH group of Fe_2O_3/BC/MXene with Pb^{2+} and MB as well as the simultaneous removal of lead and MB (Fig. S7(c)†).

3.2.9. Comparative analysis. The adsorption of Pb^{2+} by different previously reported virgin and engineered BC materials were compared with the present research. The Fe_2O_3/BC/MXene composite showed the highest sorption capacity, suggesting that the prepared Fe_2O_3/BC/MXene composite is a promising adsorbent for the removal of Pb^{2+} and MB from wastewater, with wide practical applications (Table 1).

4. Conclusions

We prepared and characterized magnetic BC resulting from the modification of *S. faguetiana* BC with Fe_2O_3 NPs and MXene. The characterization showed that the targeted engineered BC was prepared successfully and further investigations showed its high adsorption and rapid sorption rate for the removal of lead and MB from wastewater. The q_m value was 992 and 899.03 mg g^{-1} for Pb^{2+} and MB, respectively, at 293 K. The removal of Pb^{2+} and MB was enhanced by surface electrostatic forces and hydrogen bonding. The simulation of the interaction between the composite and Pb^{2+} and MB using sorption isotherms and kinetics showed that the sorption process fitted a PSO kinetic model and the Langmuir isothermal model, suggesting the single-layer sorption of Pb^{2+} and MB onto the Fe_2O_3/BC/MXene composite.

Author contributions

Aysha Bukhari: conceptualization and supervision, writing original draft, writing reviewing and editing, Irfan Ijaz: conceptualization, methodology, writing original draft, writing reviewing and editing, Ammara Nazir: data curation and investigation, Sajjad Hussain: data curation and methodology, Hina Zain: data curation and investigation, Ezaz Gilani: resource, Ahmad A. lfseisi: conceptualization and methodology, and Hijaz Ahmad: methodology and investigation.

Conflicts of interest

The authors declare that they have no known competing financial interests or personal relationships that could have appeared to influence the work reported in this paper.

Acknowledgements

The authors are grateful to the Researchers Supporting Project Number RSPD2024R669, King Saud University, Riyadh, Saudi Arabia for financial support.

References

1 R. M. J. T. economic, history review Hartwell, The causes of the industrial revolution: an essay in methodology, *Econ. Hist. Rev.*, 1965, **18**, 164–182.
2 R. Szostak, *Role of Transportation in the Industrial Revolution: A Comparison of England and France*, McGill-Queen's Press-MQUP, 1991.
3 M. Das, M. K. Ahmed, M. S. Islam, M. M. Islam, M. S. J. T. Akter and A. E. Toxicology, Heavy metals in industrial effluents (tannery and textile) and adjacent rivers of Dhaka city, Bangladesh, *Terr. Aquat.*, 2011, **5**, 8–13.
4 V. Kumar, A. K. Chopra, S. Srivastava, V. Tomar, R. K. Thakur and J. Singh, Impact of glass industry effluent disposal on soil characteristics in Haridwar region, *J. Environ. Heal. Sci.*, 2016, **2**, 1–10.
5 V. Kumar and A. K. Chopra, Heavy metals accumulation in soil and agricultural crops grown in the province of Asahi India Glass Ltd., Haridwar (Uttarakhand), India, *Adv. Crop Sci. Technol.*, 2015, 1–6.
6 M. M. Ali, M. L. Ali, M. S. Islam and M. Z. Rahman, Preliminary assessment of heavy metals in water and sediment of Karnaphuli River, Bangladesh, *Environ. Nanotechnol., Monit. Manage.*, 2016, **5**, 27–35.
7 A. E. Duncan, N. de Vries and K. B. Nyarko, Assessment of heavy metal pollution in the sediments of the River Pra and its tributaries, *Water, Air, Soil Pollut.*, 2018, **229**, 1–10.

8 J. Ifthikar, T. Wang, A. Khan, A. Jawad, T. Sun, X. Jiao, Z. Chen, J. Wang, Q. Wang, H. Wang and A. Jawad, Highly Efficient Lead Distribution by Magnetic Sewage Sludge Biochar: Sorption Mechanisms and Bench Applications, *Bioresour. Technol.*, 2017, **238**, 399–406.

9 C. Winder, Lead, reproduction and development, *Neurotoxicology*, 1993, **14**, 303–317.

10 G. Assennato, C. Paci, M. E. Baser, R. Molinini, R. G. Candela, B. M. Altamura and R. Giorgino, Sperm count suppression without endocrine dysfunction in lead-exposed men, *Arch. Environ. Health*, 1987, **42**, 124–127.

11 M. S. Barats, H. C. Gonick, S. Rothenberg, M. Balabanian and W. I. Manton, Severe lead-induced peripheral neuropathy in a dialysis patient, *Am. J. Kidney Dis.*, 2000, **35**, 963–968.

12 M. F. Bouchard, D. C. Bellinger, J. Weuve, J. Matthews-Bellinger, S. E. Gilman, R. O. Wright, J. Schwartz and M. G. Weisskopf, Blood lead levels and major depressive disorder, panic disorder, and generalized anxiety disorder in US young adults, *Arch. Gen. Psychiatry*, 2009, **66**, 1313–1319.

13 B. C. Campbell, H. L. Elliott and P. A. Meredith, Lead exposure and renal failure: does renal insufficiency influence lead kinetics, *Toxicol. Lett.*, 1981, **9**, 121–124.

14 C. Fenga, S. Gangemi, A. Alibrandi, C. Costa and E. Micali, Relationship between lead exposure and mild cognitive impairment, *G. Ig. Med. Prev.*, 2016, **57**, E205.

15 A. Alvera, E. Baştürka, L. Altaşb and M. Işıkb, A solution of taste and odor problem with activated carbon adsorption in drinking water: detailed kinetics and isotherms, *Desalin. Water Treat.*, 2022, **252**, 300–318.

16 E. Baştürk and A. Alver, Modeling azo dye removal by sono-fenton processes using response surface methodology and artificial neural network approaches, *J. Environ. Manage.*, 2019, **248**, 109300.

17 E. Basturk and M. Karatas, Advanced oxidation of reactive blue 181 solution: A comparison between fenton and sono-fenton process, *Ultrason. Sonochem.*, 2014, **21**, 1881–1885.

18 E. Basturk and M. Karatas, Decolorization of antraquinone dye Reactive Blue 181 solution by UV/H_2O_2 process, *J. Photochem. Photobiol., A*, 2015, **299**, 67–72.

19 E. Baştürk, M. Işık and M. Karakaş, Usage of Titanium Nanomaterial for the Decolorization of Methylene Blue and Reactive Red 198 Dyes by Sonocatalysis, *Desalin. Water Treat.*, 2021, **224**, 389–394.

20 A. Ebrahimian Pirbazari, E. Saberikhah, M. Badrouh and M. S. Emami, Alkali treated Foumanat tea waste as an efficient adsorbent for methylene blue adsorption from aqueous solution, *Water Resour. Ind.*, 2014, **6**, 64–80.

21 A. Ngambia, J. Ifthikar, I. I. Shahib, A. Jawad, A. Shahzad, M. Zhao, J. Wang, Z. Chen and Z. Chen, Adsorptive purification of heavy metal contaminated wastewater with sewage sludge derived carbon-supported Mg(II) composite, *Sci. Total Environ.*, 2019, **691**, 306–321.

22 A. Alver, E. Baştürk, Ş. Tulun and İ. Şimşek, Adaptive neuro-fuzzy inference system modeling of 2, 4-dichlorophenol adsorption on wood-based activated carbon, *Environ. Prog. Sustainable Energy*, 2020, **39**, e13413.

23 E. Basturk, M. Işık and M. Karatas, Removal of aniline (Methylene Blue) and azo (Reactive Red 198) dyes by photocatalysis *via* nano TiO_2, *Desalin. Water Treat.*, 2019, **143**, 306–313.

24 M. Agarwal and W. R. Singh, Desalination, Heavy metal removal from wastewater using various adsorbents: a review, *J. Water Reuse Desalin.*, 2017, **7**, 387–419.

25 G. Al-Enezi, M. F. Hamoda and N. Fawzi, Ion exchange extraction of heavy metals from wastewater sludges, *J. Environ. Sci. Health, Part A: Toxic/Hazard. Subst. Environ. Eng.*, 2004, **39**, 455–464.

26 C. Blöcher, J. Dorda, V. Mavrov, H. Chmiel, N. K. Lazaridis and K. A. Matis, Hybrid flotation—membrane filtration process for the removal of heavy metal ions from wastewater, *Water Res.*, 2003, **37**, 4018–4026.

27 J. P. Chen and L. L. Lim, Recovery of precious metals by an electrochemical deposition method, *Chemosphere*, 2005, **60**, 1384–1392.

28 Z. Djedidi, M. Bouda, M. A. Souissi, R. Ben Cheikh, G. Mercier, R. D. Tyagi and J.-F. Blais, Metals removal from soil, fly ash and sewage sludge leachates by precipitation and dewatering properties of the generated sludge, *J. Hazard. Mater.*, 2009, **172**, 1372–1382.

29 A. Jakob, S. Stucki and R. P. Struis, Complete heavy metal removal from fly ash by heat treatment: influence of chlorides on evaporation rates, *Environ. Sci. Technol.*, 1996, **30**, 3275–3283.

30 H. Ozaki, K. Sharma and W. J. D. Saktaywin, Performance of an ultra-low-pressure reverse osmosis membrane (ULPROM) for separating heavy metal: effects of interference parameters, *Desalination*, 2002, **144**, 287–294.

31 J. Rubio, M. L. Souza and R. W. Smith, Overview of flotation as a wastewater treatment technique, *Miner. Eng.*, 2002, **15**, 139–155.

32 D. Sakhi, Y. Rakhila, A. Elmchaouri, M. Abouri, S. Souabi and A. Jada, Optimization of coagulation flocculation process for the removal of heavy metals from real textile wastewater, in *Int. Conf. Adv. Intell. Syst. Sustain. Dev.*, Springer, 2018, pp. 257–266.

33 Y. Vasseghian, E.-N. Dragoi, F. Almomani and M. Berkani, Innovation, Graphene-based membrane techniques for heavy metal removal: A critical review, *Environ. Technol. Innovation*, 2021, **24**, 101863.

34 B. Renu, M. Agarwal and K. Singh, Methodologies for removal of heavy metal ions from wastewater: an overview, *Interdiscip. Environ. Rev.*, 2017, **18**, 124–142.

35 F. Marrakchi, B. H. Hameed and M. Bouaziz, Mesoporous and high-surface-Area activated carbon from defatted olive cake by-products of olive mills for the adsorption kinetics and isotherm of methylene blue and acid blue 29, *J. Environ. Chem. Eng.*, 2020, **8**, 104199.

36 B. Wang, B. Gao and Y. Wan, Comparative study of calcium alginate, ball-milled biochar, and their composites on aqueous methylene blue adsorption, *Environ. Sci. Pollut. Res.*, 2019, **26**, 11535–11541.

37 J. Ifthikar, X. Jiao, A. Ngambia, T. Wang, A. Khan, A. Jawad, Q. Xue, L. Liu and Z. Chen, Facile One-Pot Synthesis of Sustainable Carboxymethyl Chitosan – Sewage Sludge Biochar for Effective Heavy Metal Chelation and Regeneration, *Bioresour. Technol.*, 2018, **262**, 22–31.

38 Y. Zhang, G. Shi, W. Wu, A. Ali, H. Wang, Q. Wang, Z. Xu, W. Qi, R. Li, Z. J. C. Zhang, S. A. Physicochemical and E. Aspects, Magnetic biochar composite decorated with amino-containing biopolymer for phosphorus recovery from swine wastewater, *Colloids Surf., A*, 2022, **634**, 127980.

39 Y. Sun, S. M. Shaheen, E. F. Ali, H. Abdelrahman, B. Sarkar, H. Song, J. Rinklebe, X. Ren, Z. Zhang and Q. J. E. P. Wang, Enhancing microplastics biodegradation during composting using livestock manure biochar, *Environ. Pollut.*, 2022, **306**, 119339.

40 M. Azeem, S. M. Shaheen, A. Ali, P. G. S. A. Jeyasundar, A. Latif, H. Abdelrahman, R. Li, M. Almazroui, N. K. Niazi and A. K. Sarmah, Removal of potentially toxic elements from contaminated soil and water using bone char compared to plant-and bone-derived biochars: a review, *J. Hazard. Mater.*, 2021, 128131.

41 Q. Wang, B. Wang, X. Lee, J. Lehmann and B. Gao, Sorption and desorption of Pb (II) to biochar as affected by oxidation and pH, *Sci. Total Environ.*, 2018, **634**, 188–194.

42 C. Nzediegwu, M. A. Naeth and S. X. Chang, Lead (II) adsorption on microwave-pyrolyzed biochars and hydrochars depends on feedstock type and production temperature, *J. Hazard. Mater.*, 2021, **412**, 125255.

43 S. M. Shaheen, A. Mosa, H. Abdelrahman, N. K. Niazi, V. Antoniadis, M. Shahid, H. Song, E. E. Kwon and J. J. B. Rinklebe, Removal of toxic elements from aqueous environments using nano zero-valent iron-and iron oxide-modified biochar: a review, *Biochar*, 2022, **4**, 1–21.

44 X. Yang, S. M. Shaheen, J. Wang, D. Hou, Y. S. Ok, S.-L. Wang, H. Wang and J. Rinklebe, Elucidating the redox-driven dynamic interactions between arsenic and iron-impregnated biochar in a paddy soil using geochemical and spectroscopic techniques, *J. Hazard. Mater.*, 2022, **422**, 126808.

45 N. Puri, A. Gupta and A. Mishra, Recent advances on nano-adsorbents and nanomembranes for the remediation of water, *J. Cleaner Prod.*, 2021, **322**, 129051.

46 J. Xiao, R. Hu and G. Chen, Micro-nano-engineered nitrogenous bone biochar developed with a ball-milling technique for high-efficiency removal of aquatic Cd(II), Cu(II) and Pb(II), *J. Hazard. Mater.*, 2020, **387**, 121980.

47 R. Li, J. J. Wang, L. A. Gaston, B. Zhou, M. Li, R. Xiao, Q. Wang, Z. Zhang, H. Huang and W. J. C. Liang, An overview of carbothermal synthesis of metal–biochar composites for the removal of oxyanion contaminants from aqueous solution, *Carbon*, 2018, **129**, 674–687.

48 R. Li, H. Deng, X. Zhang, J. J. Wang, M. K. Awasthi, Q. Wang, R. Xiao, B. Zhou, J. Du and Z. Zhang, High-efficiency removal of Pb (II) and humate by a CeO2–MoS2 hybrid magnetic biochar, *Bioresour. Technol.*, 2019, **273**, 335–340.

49 R. Li, Y. Zhang, H. Deng, Z. Zhang, J. J. Wang, S. M. Shaheen, R. Xiao, J. Rinklebe, B. Xi and X. He, Removing tetracycline and Hg (II) with ball-milled magnetic nanobiochar and its potential on polluted irrigation water reclamation, *J. Hazard. Mater.*, 2020, **384**, 121095.

50 Y. Luo, K. Xie, Y. Feng, Q. He, K. Zhang, S. Shen, F. J. C. Wang, S. A. Physicochemical and E. Aspects, Synthesis of a $La(OH)_3$ nanorod/walnut shell biochar composite for reclaiming phosphate from aqueous solutions, *Colloids Surf., A*, 2021, **610**, 125736.

51 Y. Peng, M. Azeem, R. Li, L. Xing, Y. Li, Y. Zhang, Z. Guo, Q. Wang, H. H. Ngo and G. Qu, Zirconium hydroxide nanoparticle encapsulated magnetic biochar composite derived from rice residue: Application for As(III) and As(V) polluted water purification, *J. Hazard. Mater.*, 2022, **423**, 127081.

52 Z. Shen, J. Zhang, D. Hou, D. C. W. Tsang, Y. S. Ok and D. Alessi, Synthesis of MgO-coated corncob biochar and its application in lead stabilization in a soil washing residue, *Environ. Int.*, 2019, **122**, 357–362.

53 X. Su, Y. Guo, L. Yan, Q. Wang, W. Zhang, X. Li, W. Song, Y. Li and G. Liu, MoS_2 nanosheets vertically aligned on biochar as a robust peroxymonosulfate activator for removal of tetracycline, *Sep. Purif. Technol.*, 2022, **282**, 120118.

54 P. Wu, P. Cui, Y. Zhang, M. E. Alves, C. Liu, D. Zhou and Y. J. Wang, Unraveling the molecular mechanisms of Cd sorption onto MnOx-loaded biochar produced from the Mn-hyperaccumulator Phytolacca americana, *J. Hazard. Mater.*, 2022, **423**, 127157.

55 A. Briso, G. Quintana, V. Ide, C. Basualto, L. Molina, G. Montes and F. Valenzuela, Integrated use of magnetic nanostructured calcium silicate hydrate and magnetic manganese dioxide adsorbents for remediation of an acidic mine water, *J. Water Process Eng.*, 2018, **25**, 247–257.

56 A. Foroughnia, A. D. Khalaji, E. Kolvari and N. Koukabi, Synthesis of new chitosan Schiff base and its Fe_2O_3 nanocomposite: Evaluation of methyl orange removal and antibacterial activity, *Int. J. Biol. Macromol.*, 2021, **177**, 83–91.

57 J. Ifthikar, Z. Chen, Z. Chen and A. Jawad, A self-gating proton-coupled electron transfer reduction of hexavalent chromium by core-shell SBA-Dithiocarbamate chitosan composite, *J. Hazard. Mater.*, 2020, **384**, 121257.

58 L. Shen, J. Wang, Z. Li, L. Fan, R. Chen, X. Wu, J. Li and W. Zeng, A high-efficiency Fe_2O_3@ Microalgae composite for heavy metal removal from aqueous solution, *J. Water Process Eng.*, 2020, **33**, 101026.

59 E. Ragab, M. Shaban, A. A. Khalek and F. Mohamed, Design and characterization of PANI/starch/Fe_2O_3 bio composite for wastewater remediation, *Int. J. Biol. Macromol.*, 2021, **181**, 301–312.

60 A. K. Geim and K. S. Novoselov, The rise of graphene, *Nat. Mater.*, 2010, 11–19.

61 C. N. R. Rao, A. K. Sood, K. S. Subrahmanyam and A. Govindaraj, Graphene: the new two-dimensional nanomaterial, *Angew. Chemie.*, 2009, **48**, 7752–7777.

62 F. Cao, Y. Zhang, H. Wang, K. Khan, A. K. Tareen, W. Qian, H. Zhang and H. J. A. M. Ågren, Recent Advances in

Oxidation Stable Chemistry of 2D MXenes, *Adv. Mater.*, 2022, **34**, 2107554.

63 P. Ma, D. Fang, Y. Liu, Y. Shang, Y. Shi and H. Y. Yang, MXene-Based Materials for Electrochemical Sodium-Ion Storage, *Adv. Mater.*, 2021, **8**, 2003185.

64 L. Qin, Q. Tao, X. Liu, M. Fahlman, J. Halim, P. O. Å. Persson, J. Rosen and F. Zhang, Polymer-MXene composite films formed by MXene-facilitated electrochemical polymerization for flexible solid-state microsupercapacitors, *Nano Energy*, 2019, **60**, 734–742.

65 H. Shin, W. Eom, K. H. Lee, W. Jeong, D. J. Kang and T. H. Han, Highly Electroconductive and Mechanically Strong $Ti_3C_2T_x$ MXene Fibers Using a Deformable MXene Gel, *ACS Nano*, 2021, **15**, 3320–3329.

66 S. P. Sreenilayam, I. U. Ahad, V. Nicolosi and D. Brabazon, MXene materials based printed flexible devices for healthcare, biomedical and energy storage applications, *Mater. Today*, 2021, **43**, 99–131.

67 M. Malaki, A. Maleki and R. S. Varma, MXenes and ultrasonication, *J. Mater. Chem. A*, 2019, **7**, 10843–10857.

68 X. Wu, M. Ding, H. Xu, W. Yang, K. Zhang, H. Tian, H. Wang and Z. Xie, Scalable $Ti_3C_2T_x$ MXene interlayered forward osmosis membranes for enhanced water purification and organic solvent recovery, *ACS Nano*, 2020, **14**, 9125–9135.

69 F. Kong, X. He, Q. Liu, X. Qi, D. Sun, Y. Zheng, R. Wang and Y. Bai, Further surface modification by carbon coating for in-situ growth of Fe3O4 nanoparticles on MXene Ti_3C_2 multilayers for advanced Li-ion storage, *Electrochim. Acta*, 2018, **289**, 228–237.

70 E. Paulson and M. Jothibas, Significance of thermal interfacing in hematite (α-Fe_2O_3) nanoparticles synthesized by sol-gel method and its characteristics properties, *Surf. Interfaces*, 2021, **26**, 101432.

71 C. N. C. Hitam and A. A. Jalil, A review on exploration of Fe_2O_3 photocatalyst towards degradation of dyes and organic contaminants, *J. Environ. Manage.*, 2020, **258**, 110050.

72 H. Shan, C. Zeng, C. Zhao and H. Zhan, Iron oxides decorated graphene oxide/chitosan composite beads for enhanced Cr(VI) removal from aqueous solution, *Int. J. Biol. Macromol.*, 2021, **172**, 197–209.

73 W. Feng, H. Luo, Y. Wang, S. Zeng, L. Deng, X. Zhou, H. Zhang and S. Peng, Ti_3C_2 MXene: a promising microwave absorbing material, *RSC Adv.*, 2018, **8**, 2398–2403.

74 M. Qi, L. Lin, L. Wang, Z. Bai, Y. Yu, J. Gu and Y. Liu, Spindle $MnCO_3$ tightly encapsulated by MXene nanoflakes with strengthened interface effect for lithium-ion battery, *Surf. Coat. Technol.*, 2021, **417**, 127192.

75 Y. Shen, Q. Fang and B. Chen, Environmental applications of three-dimensional graphene-based macrostructures: adsorption, transformation, and detection, *Environ. Sci. Technol.*, 2015, **49**, 67–84.

76 Q. Wu, Y. Xian, Z. He, Q. Zhang, J. Wu, G. Yang, X. Zhang, H. Qi, J. Ma, Y. Xiao and L. Long, Adsorption characteristics of Pb(II) using biochar derived from spent mushroom substrate, *Sci. Rep.*, 2019, **9**, 1–11.

77 C. A. Guerrero-Fajardo, L. Giraldo and J. C. Moreno-Piraján, Preparation and characterization of graphene oxide for Pb(II) and Zn(II) ions adsorption from aqueous solution: Experimental, thermodynamic and kinetic study, *Nanomaterials*, 2020, **10**, 1022.

78 T. Bahadir, İ. Şimşek, Ş. Tulun and H. Çelebi, Use of different food wastes as green biosorbent: isotherm, kinetic, and thermodynamic studies of Pb^{2+}, *Environ. Sci. Pollut. Res.*, 2023, **30**, 103324–103338.

79 E. Mosaffa, A. Banerjee and H. Ghafuri, Sustainable high-efficiency removal of cationic and anionic dyes using new super adsorbent biochar: performance, isotherm, kinetic and thermodynamic evaluation, *Environ. Sci.: Water Res. Technol.*, 2023, **9**, 2643–2663.

80 Y. Li, J. Shao, X. Wang, H. Yang, Y. Chen, Y. Deng, S. Zhang and H. Chen, Upgrading of bio-oil: Removal of the fermentation inhibitor (furfural) from the model compounds of bio-oil using pyrolytic char, *Energy Fuels*, 2013, **27**, 5975–5981.

81 S. A. Dzuba, D. V. Leonov and N. V. Surovtsev, Membrane-sugar interactions probed by low-frequency raman spectroscopy: The monolayer adsorption model, *Langmuir*, 2020, **36**, 11655–11660.

82 M. Shafiee, R. Foroutan, K. Fouladi, M. Ahmadlouydarab, B. Ramavandi and S. Sahebi, Application of oak powder/Fe_3O_4 magnetic composite in toxic metals removal from aqueous solutions, *Adv. Powder Technol.*, 2019, **30**, 544–554.

83 Y. Huang, H. Zheng, X. Hu, Y. Wu, X. Tang, Q. He and S. Peng, Enhanced selective adsorption of lead (II) from complex wastewater by DTPA functionalized chitosan-coated magnetic silica nanoparticles based on anion-synergism, *J. Hazard. Mater.*, 2022, **422**, 126856.

84 M. F. El-Banna, A. Mosa, B. Gao, X. Yin, Z. Ahmad and H. Wang, Sorption of lead ions onto oxidized bagasse-biochar mitigates Pb-induced oxidative stress on hydroponically grown chicory: Experimental observations and mechanisms, *Chemosphere*, 2018, **208**, 887–898.

85 Y. Li, S. M. Shaheen, M. Azeem, L. Zhang, C. Feng, J. Peng, W. Qi, J. Liu, Y. Luo and Y. Peng, Removal of lead (Pb^{2+}) from contaminated water using a novel MoO3-biochar composite: Performance and mechanism, *Environ. Pollut.*, 2022, **308**, 119693.

86 S. Wan, J. Wu, S. Zhou, R. Wang, B. Gao and F. He, Enhanced lead and cadmium removal using biochar-supported hydrated manganese oxide (HMO) nanoparticles: Behavior and mechanism, *Sci. Total Environ.*, 2018, **616**, 1298–1306.

87 D. Mohan, H. Kumar, A. Sarswat, M. Alexandre-Franco and C. U. Pittman Jr, Cadmium and lead remediation using magnetic oak wood and oak bark fast pyrolysis bio-chars, *Chem. Eng. J.*, 2014, **236**, 513–528.

88 F. Marrakchi, M. Bouaziz and B. H. Hameed, Adsorption of acid blue 29 and methylene blue on mesoporous K_2CO_3-activated olive pomace boiler ash, *Colloids Surf., A.*, 2017, **535**, 157–165.

89 E. Kalipci, Removal of methylene blue from aqueous solutions with natural olive pomace modified with ultrasounds and acid, *Environ. Prot. Eng.*, 2016, **42**, 5–17.

90 X. J. Liu, M. F. Li and S. K. Singh, Manganese-modified lignin biochar as adsorbent for removal of methylene blue, *J. Mater. Res. Technol.*, 2021, **12**, 1434–1445.

91 H. Zeng, W. Qi, L. Zhai, F. Wang, J. Zhang and D. Li, Magnetic biochar synthesized with waterworks sludge and sewage sludge and its potential for methylene blue removal, *J. Environ. Chem. Eng.*, 2021, **9**, 105951.